Pure Appl. Geophys. 174 (2017), 875–893

DOI 10.1007/s00024-016-1445-2

Pure and Applied Geophysics

Solving for Source Parameters Using Nested Array Data: A Case Study from the Canterbury, New Zealand Earthquake Sequence

Corrie Neighbors,[1,2] E. S. Cochran,[3] K. J. Ryan,[4] and A. E. Kaiser[5]

Abstract—The seismic spectrum can be constructed by assuming a Brune spectral model and estimating the parameters of seismic moment (M_0), corner frequency (f_c), and high-frequency site attenuation (κ). Using seismic data collected during the 2010–2011 Canterbury, New Zealand, earthquake sequence, we apply the non-linear least-squares Gauss–Newton method, a deterministic downhill optimization technique, to simultaneously determine the M_0, f_c, and κ for each event-station pair. We fit the Brune spectral acceleration model to Fourier-transformed S-wave records following application of path and site corrections to the data. For each event, we solve for a single M_0 and f_c, while any remaining residual kappa, κ_r, is allowed to differ per station record to reflect varying high-frequency falloff due to path and site attenuation. We use a parametric forward modeling method, calculating initial M_0 and f_c values from the local GNS New Zealand catalog $M_{w,\ GNS}$ magnitudes and measuring an initial κ_r using an automated high-frequency linear regression method. Final solutions for M_0, f_c, and κ_r are iteratively computed through minimization of the residual function, and the Brune model stress drop is then calculated from the final, best-fit f_c. We perform the spectral fitting routine on nested array seismic data that include the permanent GeoNet accelerometer network as well as a dense network of nearly 200 Quake Catcher Network (QCN) MEMs accelerometers, analyzing over 180 aftershocks $M_{w,GNS} \geq 3.5$ that occurred from 9 September 2010 to 31 July 2011. QCN stations were hosted by public volunteers and served to fill spatial gaps between existing GeoNet stations. Moment magnitudes determined using the spectral fitting procedure ($M_{w,SF}$) range from 3.5 to 5.7 and agree well with $M_{w,GNS}$, with a median difference of 0.09 and 0.17 for GeoNet and QCN records, respectively, and 0.11 when data from both networks are combined. The majority of events are calculated to have stress drops between 1.7 and 13 MPa (20th and 80th percentile, correspondingly) for the combined networks. The overall median stress drop for the combined networks is 3.2 MPa, which is similar to median stress drops previously reported for the Canterbury sequence. We do not observe a correlation between stress drop and depth for this region, nor a relationship between stress drop and magnitude over the catalog considered. Lateral spatial patterns in stress drop, such as a cluster of aftershocks near the eastern extent of the Greendale fault with higher stress drops and lower stress drops for aftershocks of the 2011 $M_{w,GNS}$ 6.2 Christchurch mainshock, are found to be in agreement with previous reports. As stress drop is arguably a method-dependent calculation and subject to high spatial variability, our results using the parametric Gauss–Newton algorithm strengthen conclusions that the Canterbury sequence has stress drops that are more similar to those found in intraplate regions, with overall higher stress drops that are typically observed in tectonically active areas.

Key words: Canterbury earthquake sequence, strong ground motion, quake-catcher network, MEMs accelerometers, nested array, Gauss–Newton method, Brune model, spectral acceleration, stress drop.

1. Introduction

It is well known that the seismic ground motions observed at a given location are the result of the convolution of source, path, and site terms. Understanding the relative contributions of the source, path, and site to the observed ground motions is critical for probing the characteristics of seismic sources in a sequence and/or region, as well as for more practical applications such as seismic hazard assessment. The earthquake source parameters of seismic moment (M_0) and corner frequency (f_c) are commonly determined from local records assuming a spectral source model (e.g., Brune 1970, 1971), while the path propagation and near-surface site response parameter, kappa (κ), are estimated from the high-frequency spectral decay. The source, path, and site terms are typically considered frequency dependent, in the sense that the seismic moment of the source is obtained from the low-frequency portion of the spectrum, and path and site factors typically influence

Electronic supplementary material The online version of this article (doi:10.1007/s00024-016-1445-2) contains supplementary material, which is available to authorized users.

[1] University of California, Riverside, CA 92521, USA. E-mail: corrie.neighbors@wnmu.edu

[2] *Present Address*: Western New Mexico University, Silver City, NM 88061, USA.

[3] U.S. Geological Survey, Pasadena, CA 91106, USA.

[4] U.S. Geological Survey, Menlo Park, CA 94025, USA.

[5] GNS Science, Lower Hutt, New Zealand.

relatively higher frequencies. However, in practice, the relevant frequencies for determining source and attenuation terms are not wholly independent, so it can be difficult to constrain the contributions of these varying seismic characteristics (Anderson and Hough 1984; Anderson 1986; Abercrombie 1995; Kilb et al. 2012; Ko et al. 2012), particularly in tectonically and geologically complex regions.

Analysis of the earthquake spectrum can yield significant tradeoffs between the source corner frequency and path–site attenuation (e.g., Ko et al. 2012) where a strong decay of high-frequency energy may result in underestimation of the corner frequency (Anderson 1986). To constrain this tradeoff, studies that use a grid search to determine the source, path, and site terms hold one parameter fixed—typically the corner frequency—and solve for other terms (e.g., moment magnitude, apparent geometric spreading, frequency-dependent path attenuation, site attenuation; Anderson and Humphrey 1991). The value assigned to the fixed term may introduce bias into the solution of the other parameters (Liu et al. 1994); thus, other methods, such as spectral inversions of empirical Green's function deconvolutions (e.g., Hough 1997), were adopted to provide a more independent approach. However, these methods may be hampered by limitations in bandwidth or the availability of spatially clustered, highly cross-correlated events (e.g., Abercrombie 2015). Other methods simultaneously invert for source, path and site contributions using non-parametric approaches (e.g., Castro et al. 1990; Oth et al. 2011). These methods can provide independent estimates of the spectral parameters, but inverse problems may be ill conditioned and solutions may be non-unique.

Here, we explore the feasibility of using the iterative Gauss–Newton method to fit the Brune model to the earthquake spectra from which we can determine earthquake source and site parameters. The Gauss–Newton global downhill optimization method is ideal for solving non-linear least-squares problems and, while this method has been successfully applied to other non-linear problems in geophysics (e.g., Hicks and Pratt 2001; Sheen et al. 2006; Alpak et al. 2011), it has not been extensively used in this application (e.g., Taylor and Hartse 1998; Imanishi et al. 2004; Drouet et al. 2010). The Gauss–Newton algorithm is shown to be computationally efficient and can provide optimal solutions when there are suitable constraints on the initial values for the parameters of interest; however, it remains in contrast to a combined stochastic and deterministic method, such as the Markov chain Monte Carlo simulation, which has little reliance on initial conditions, but can be much more computationally expensive (e.g., Chen et al. 2008). Thus, to determine the applicability of the Gauss–Newton method for spectral modeling, we start with initial best guess parameters (M_0, f_c, and κ_r) and, through an iterative method based on the Jacobian matrix of partial derivatives of the residual function, test for convergence accuracy and precision for best-fit M_0, f_c, κ_r values.

For this case study, we examine aftershock data acquired following 2010 M_w 7.2 Darfield, New Zealand mainshock (Gledhill et al. 2011; Bannister et al. 2011). The sequence included the M_w 6.2 Christchurch earthquake, which caused significant site effects (e.g., site amplification and liquefaction) and structural damage in the Christchurch region (e.g., Kaiser et al. 2012). Notably, the M_w 6.2 event produced near-field peak ground accelerations greater than 2 g (Fry et al. 2011b) and complex site response attributed to the lithology, hydrogeology, and geometry of the Christchurch basin (Fry et al. 2011a; Kaiser et al. 2012). This productive sequence has been extensively studied using the strong-motion GeoNet network. The GeoNet seismic network (Peterson et al. 2011) comprises the New Zealand National Seismograph Network (NZNSN) and the New Zealand National Strong Motion Network, the latter of which consists of 222 sites across New Zealand (http://www.geonet.org.nz).

Adding to the data acquired by the permanent GeoNet array, the early aftershock period was recorded by the Quake Catcher Network's (QCN) temporary Rapid Aftershock Mobilization Program (RAMP) deployment. QCN is a volunteer computing network composed of small, low cost (<$50) micro-electro-mechanical systems (MEMS) accelerometers, which can be stationed to create high-density arrays at the fraction of the cost of a traditional seismic network (Cochran et al. 2009). QCN sensors are considered Class C sensors (Evans et al. 2005), as MEMS sensors are lower resolution than traditional

sensors, ranging from 10-bit to 16-bit resolution. Ideally, these MEMs sensors can be utilized to increase spatial station density when "nested" among a sparsely instrumented Class A network (i.e., $\geq$20 bit resolution) to address earthquake engineering (e.g., site and building response), earthquake early warning, and other seismic investigations. Since QCN's inception in 2007, studies have been undertaken to explore the utility of such a low cost network, including optimizing the software design (Cochran et al. 2009; Benson et al. 2013), verifying MEMS sensor performance (Cochran et al. 2011; Evans et al. 2014), and advancing event detection and characterization techniques (Chung et al. 2011, 2015; Lawrence et al. 2014; Yildirim et al. 2015; Dominguez et al. 2015). Beyond event detection, Neighbors et al. (2015) show that estimates of the high-frequency attenuation parameter (κ) determined using low-resolution 12-bit QCN sensors compare favorably to broadband data recorded during M 8.8 Maule, Chile aftershock sequence.

For the RAMP in New Zealand, predominantly 14-bit JoyWarrior QCN sensors were deployed with digital resolutions of 2.4×10^{-3} m/s^2, compared to 24-bit GeoNet accelerometers with several orders of magnitude higher resolution (4.7×10^{-6} m/s^2). These sensors have undergone bench test simulations and perform within ANSS Class C sensor standards (Evans et al. 2014). During the RAMP, nearly 200 accelerometers were deployed, predominantly on the ground floors of local buildings and residences in the greater Christchurch region (Cochran et al. 2011). While QCN station placement is predominantly a function of host availability, neighborhoods in Christchurch were targeted to increase spatial density and investigate the complex site response observed during the early aftershock sequence. QCN stations captured over 155 aftershocks of $3.6 \geq M_w \leq 6.2$ from 9 September 2010 to 31 July 2011 recording a large volume of data (over 14,600 horizontal component records). Using these data Cochran et al. (2011) shows that horizontal component acceleration response spectra of the QCN MEMs sensors are very similar to nearby GeoNet stations (e.g., as short as 200 m nested station spacing), displaying high cross-correlation coefficients (average 0.94) for frequencies above 0.1 Hz. And, time series and acceleration spectra of the sensors compare favorably to the strong-motion 24-bit GeoNet sensors (Kaiser et al. 2013). The recent works by Lawrence et al. (2014) and Chung et al. (2015) use data recorded by the QCN RAMP in New Zealand to demonstrate that improved rapid detection algorithms can obtain accurate locations and magnitudes when compared to earthquake catalogs utilizing GeoNet data.

The strong-motion data collected during the Darfield aftershock sequence by the GeoNet and QCN networks, which cover a wide range of earthquake magnitudes and distances, are ideal to perform spectral analysis to estimate source and site parameters. Previously, Oth and Kaiser (2014) used a non-parametric generalized inversion approach to solve for source spectra using only GeoNet station data. In contrast, we determine the source (M_0, f_c) and, after correcting for path and site attenuation effects, any residual site (κ_r) parameters using a parametric forward modeling approach to fit the spectral model to a larger set of GeoNet stations as well as the numerous QCN stations. We compare the spectral fit results from the individual networks, i.e., using solely GeoNet or QCN data, as well as the combined datasets to evaluate the use of low-resolution MEMS accelerometer data to recover seismic source information. We then use M_0 and f_c to estimate stress drops and compare to those previously reported for the Canterbury sequence (e.g., Oth and Kaiser 2014). Finally, we conclude by examining relationships between stress drop and magnitude and spatial distribution (depth and lateral extent).

2. Data

We use strong motion data from over 80 GeoNet stations obtained from GNS (*ftp://ftp.geonet.org.nz/strong*) (Fig. 1). The New Zealand National Strong Motion Network sites use traditional accelerometers, i.e., Kinemetrics Episensors, Kinemetrics Etnas, or Canterbury Seismic Instruments CUSP units, with dataloggers set to record triggered waveforms with sample rates of 200 Hz. We also use strong motion data from 198 QCN stations located in the greater Christchurch region (http://quakecatcher.net); sensor placement was determined largely by availability of

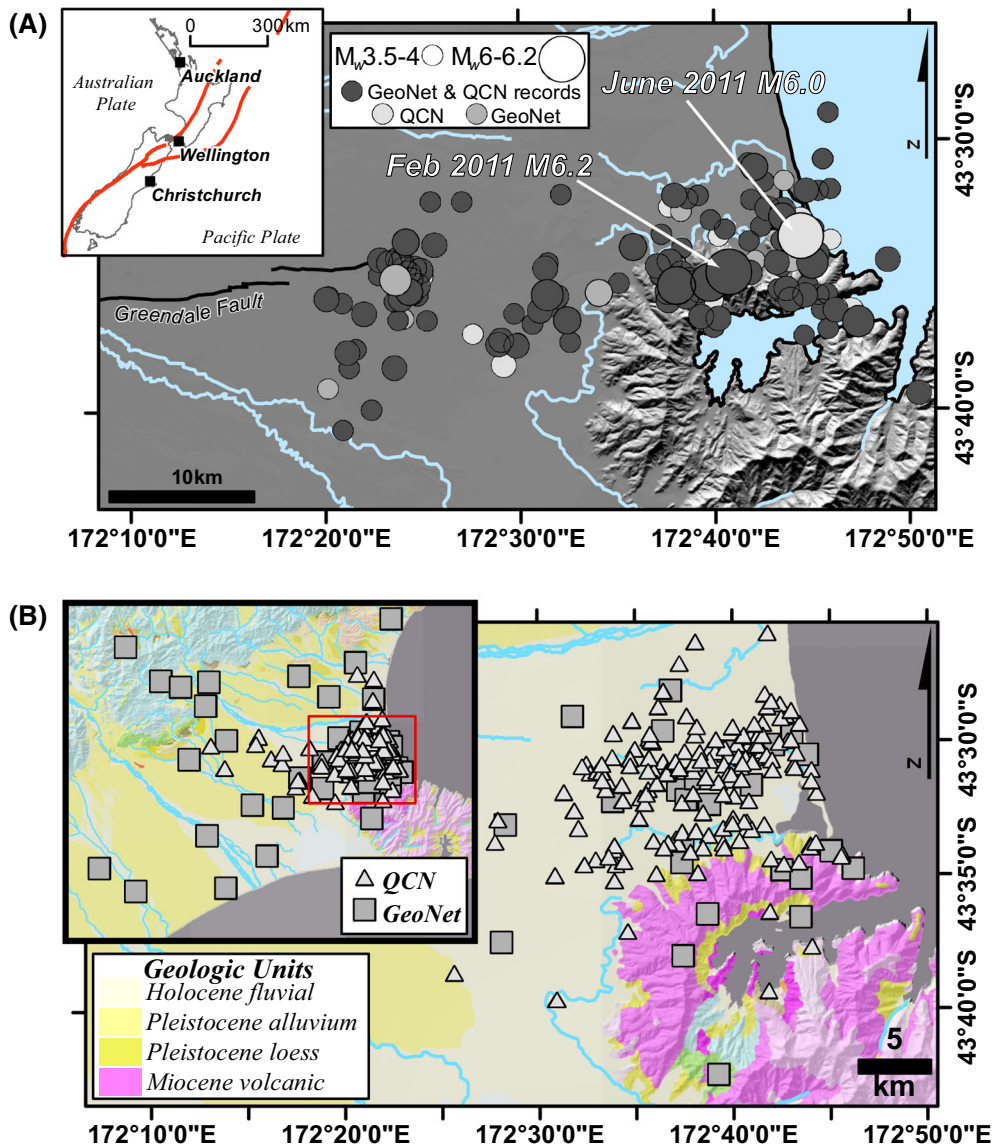

Figure 1

a Earthquakes considered in this study. Events are scaled by magnitude, M_w 3.5–6.2, such that small circles are M_w 3.5–4.0 scaling up in magnitude to the largest circles, which represent the February 2011 M_w 6.2 Christchurch and the June 2011 M_w 6.0 earthquakes. Events are colored by network data used in the analysis; events where QCN records were used appear *lightest gray*, solely GeoNet-based data are *gray*, and data from the combined networks are *darkest gray*. *Inset map* shows tectonic setting with major fault systems (i.e., Alpine Fault) shown by *red lines* and cities (*labeled squares*), including Christchurch where the study is based. **b** Station distribution of local GeoNet stations (*squares*) and QCN stations (*triangles*). Basemap reflects major geologic units in the region; the beige units are Quaternary sediment and alluvium with the pink unit representing a Miocene-age volcanic suite

volunteers to host stations (Fig. 1). Sensors were oriented and adhered to the floor of buildings and programmed to record continuously at 50 samples per second. Detailed description of the QCN acquisition methods and the New Zealand RAMP deployment can be found in Cochran et al. (2011) and Lawrence et al. (2014).

We limit the analyses to events greater than $M_{w,GNS}$ 3.5, due to QCN's lower signal-to-noise (SNR) levels at high frequencies (SNR typically

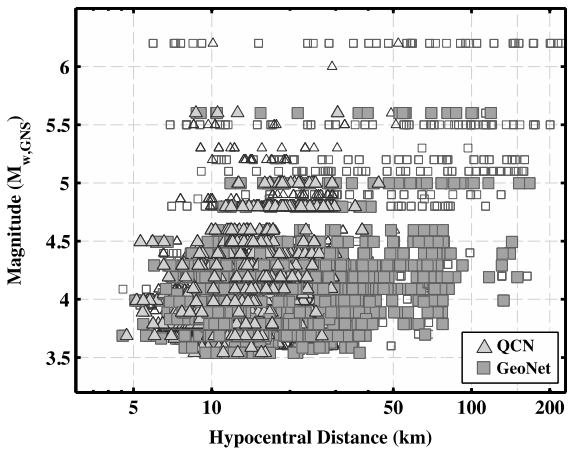

Figure 2
Plot of dataset attributes according to GNS GeoNet-based catalog magnitude ($M_{W,GNS}$) and hypocentral distance for event-station pairs meeting waveform quality criteria. *Closed symbols* denote events used in the source spectral analysis (i.e., event data met quality constraints in terms of signal-to-noise ratio (SNR) and sufficient number of recordings) and that were recorded by both GeoNet and QCN networks

degrades around 15 Hz). Additionally, we do not include events above $M_{w,GNS}$ 5.6 in our spectral analysis as f_c approaches the low-frequency extent of our windowed bandwidth, given the defined minimum window length of 2 s. Usable data from QCN stations tend to be limited to nearby events (<50 km) due to the lower resolution of sensors, while the GeoNet stations provide longer-range data (Fig. 2). All records are initially reviewed by visual inspection for clarity of body wave arrivals followed by baseline correction (removal of the mean) and manual picking of the direct S-wave arrival. Time window durations are calculated beginning at the arrival of the S-wave and ending when 80% of the S-wave energy is reached (Fig. 3). Window lengths vary, though records are excluded from further analysis if the window is shorter than 2 s. On average, GeoNet records have a window length of 5.5 s and QCN records have a window length of 6.7 s with a maximum window length of 13.6 s for both networks. Windows are tapered at the beginning and end with a cosine taper and the Fourier transform was taken to obtain the frequency spectra (Fig. 3).

3. Methods: Applying the Site Spectral Correction

During the Canterbury earthquake sequence, large amplification effects were observed in the Christchurch region, with horizontal motions amplified up to a factor of 10 at soft soil sites relative to the horizontal component of the average reference station on soft rock (Kaiser et al. 2016). Such frequency-dependent path and site effects can cause systematic overestimation of the M_0 and may bias the f_c solution during spectral modeling. Therefore, we divide the raw spectra by site-specific amplification factors over a wide frequency band, 0.6 up to 20 Hz. The low-frequency limit is chosen based on adequate signal resolution relative to sensor and ambient noise as well as consideration of the minimum resolvable frequency in our spectral dataset given the choice of window length used to calculate the spectra (i.e., 2 s). The high-frequency limit is based on the SNR for each record, as described in the following section on the spectral fitting method. We use the horizontal site response functions obtained from Kaiser et al. (2016) and Oth and Kaiser (2014) through non-parametric inversion of the Canterbury data to limit the biasing effect of local site properties on the source spectra. Site-specific amplification factors are available for most of the GeoNet stations, which correct spectra back to an average soft rock reference station in the Canterbury region. As a result, where site-specific factors are used, they should largely account for any differences in site attenuation relative to this reference station condition (but not site attenuation at the reference station itself). For all of the QCN stations and the few GeoNet stations without site-specific corrections, we use the generic average site amplification factor of Kaiser et al. (2016) for a specific surface geology classification (e.g., Holocene-age fluvial sediment and alluvium, Pleistocene-age alluvium, etc.; Online Resource 1). At QCN stations where a generic site response function is used, further differences in individual site attenuation compared to the generic site may also be represented in the spectra. Overall, the removal of site-specific amplification tends to decrease the amplitude of the low frequencies and flatten the high-frequency decay (Fig. 3). Following application of the site response functions, the spectra are uniformly re-sampled in log-

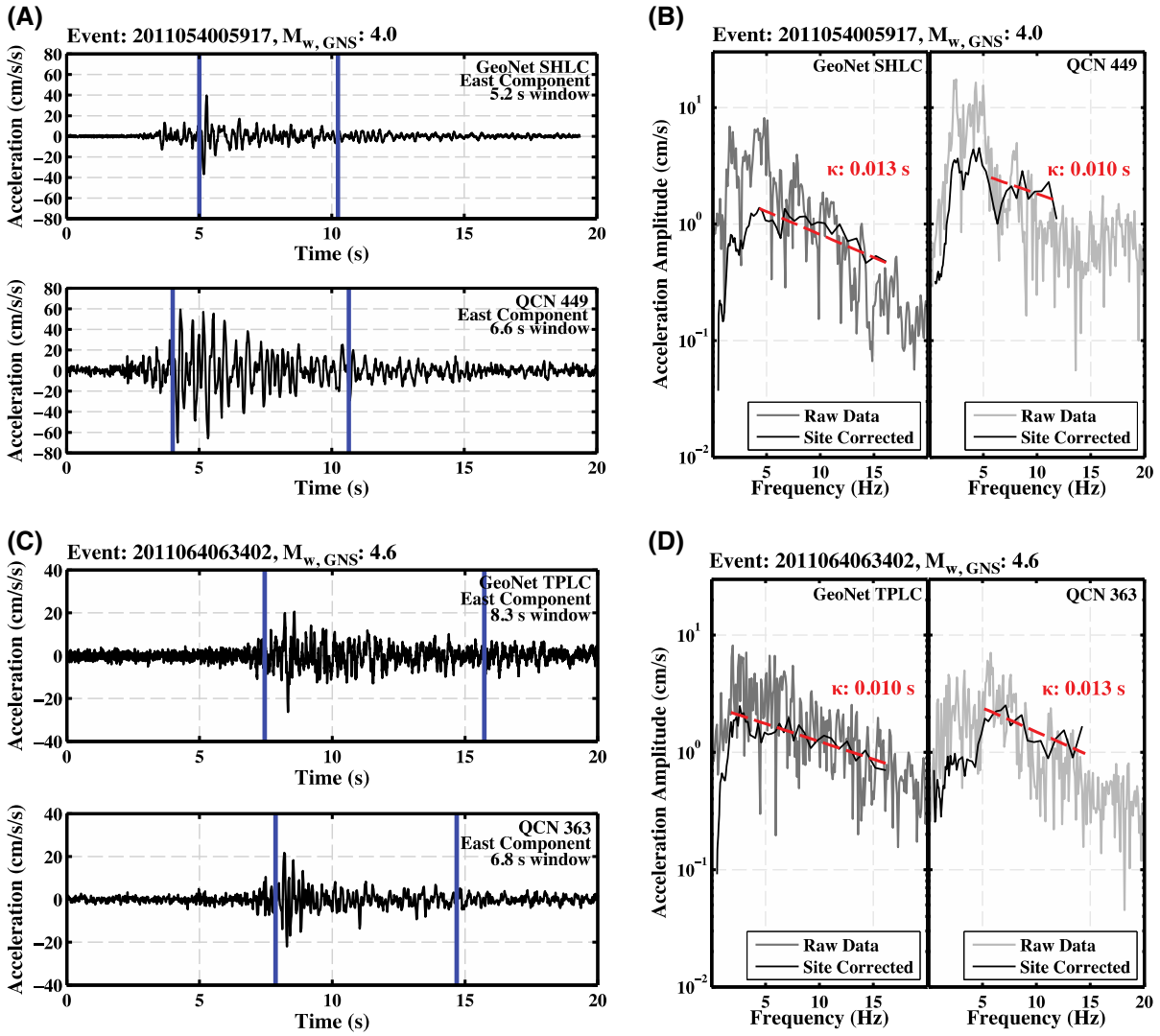

Figure 3

Plots of sample station recordings of two events used in source spectral analysis, **a** $M_{W,GNS}$ 4.0 and **c** $M_{W,GNS}$ 4.6. QCN stations are located by volunteer availability and were not co-located with GeoNet stations; however, the QCN and GeoNet station pairs shown for event (**a**, **c**) are approximately 5 km from one another on Holocene fluvial sediment sites. *Solid blue lines* in **a**, **c** indicate the length of S-wave time window used to compute acceleration amplitude spectra shown in (**b**, **d**). **b**, **d** depict both the raw spectra (*gray line*) and site corrected, smoothed spectra (*black solid line*) for the respective events. GeoNet sites have station-specific site amplification corrections while QCN use generic corrections based on geologic unit. κ estimations based on the Anderson and Hough (1984) method are shown in *red*

space and a Konno and Ohmachi (1998) filter ($b = 20$) is applied to smoothen the data.

4. Methods: Determining Initial Parameters for Forward Modeling

To derive source parameters, we assume a Brune source spectrum (Brune 1970, 1971) with an Anderson and Hough (1984) high-frequency roll-off in acceleration, such that the equation describing the spectral shape appears as (e.g., Kilb et al. 2012; Oth and Kaiser 2014):

$$M(f) = \left(\frac{\Phi V F M_0}{4\pi\rho\beta^3 r}\right) \frac{(2\pi f)^{\gamma}}{\left(1 + \left(\frac{f}{f_c}\right)^2\right)} \exp(-\pi\kappa f). \quad (1)$$

We adopt similar parameters for the Christchurch dataset as Oth and Kaiser (2014), where γ is set by

datatype (2 for spectral acceleration), Φ is the average radiation pattern of S-waves (0.55 from Boore and Boatwright 1984), β is the shear wave velocity (330,000 cm/s from Fry et al. 2014), r is source-station hypocentral distance (i.e., $1/r$, geometric spreading), V and F describe the separation of S-wave energy onto two horizontal components $\left(\frac{1}{\sqrt{2}}\right)$ and free surface effect (factor of 2), respectively, while ρ is the upper crustal density (2.7 g/cm^3).

Due to the non-linear appearance of κ in the Anderson and Hough (1984) adaptation of the Brune model, we first linearize the form of Eq. (1) with respect to κ by taking the natural logarithm. This results in

$$\ln[M(f,\kappa,r,M_0,f_c)] = \ln(A_0 M_0) + \ln\left[\frac{(2\pi f)^2}{1+\left(\frac{f}{f_c}\right)^2}\right] - \pi\kappa f, \quad (2)$$

where the A_0 term replaces the spectral amplitude constants from Eq. (1). We can then construct a forward model using best guess initial M_0, f_c, and κ parameters to compute model spectra. We determine a best guess initial M_0 from the GNS catalog $M_{w,GNS}$ by (Hanks and Kanamori 1979)

$$\log M_0 = 16.05 + 1.5 M_{w,GNS}. \quad (3)$$

For events where only local magnitudes (M_L) are available, we first convert M_L to M_w using the previously published relationship $M_w = M_L - 0.34$ for New Zealand (Ristau 2013; Oth and Kaiser 2014). Based on the results of Oth and Kaiser (2014), who found higher-than-average stress drops for the Canterbury sequence that were in the range of 1–20 MPa (10–200 bar), we assume an initial stress drop of 10 MPa (100 bar) and define the best guess initial f_c as (Eshelby 1957)

$$f_c = 0.49\left[\frac{\Delta\sigma}{M_0}\right]^{1/3}\beta. \quad (4)$$

While we require a single M_0 and f_c per event, κ_r, any residual high-frequency response present following the attenuation correction, is allowed to vary freely. κ has traditionally been labeled a site term, with higher κ associated with higher attenuation. However, recent studies have shown that κ is somewhat of a 'catch-all' term that may depend on source, path, and site effects and separating the contribution from each of these factors can be difficult (e.g., Tsai and Chen 2000; Purvance and Anderson 2003; Parolai and Bindi 2004; Ktenidou et al. 2014; Neighbors et al. 2015); therefore, we do not constrain κ_r to be station specific. We estimate a best guess initial κ_r from the high-frequency decay measured on each event-station spectral acceleration record, as defined by Anderson and Hough (1984). The initial Anderson and Hough method was developed for moderate-sized events ($>M$ 5) due to concern for the $f_c - \kappa$ tradeoff that might occur with smaller magnitude events that have theoretically higher corner frequencies; however, recent studies have successfully pushed the magnitude threshold lower [Douglas et al. (2010) for $>M$ 3.5 events in France; Fernández et al. (2010) for $>M$ 3.5 events in Mexico; Gentili and Franceschina (2011) for $>M$ 3 event in Italy]. Here, we use the Anderson and Hough method as mechanism to obtain an initial κ_r for the forward model, adopting the automated routine of Neighbors et al. (2015) to fit a linear regression to the falloff of the high frequencies. κ_r is measured above the corner frequency over a bandwidth from f_c to f_x, where f_x is the high-frequency limit defined to be where the average SNR calculated over a moving window is approximately equal to 2 and less than the Nyquist frequency. Typically an SNR of 3 is used to define the frequency band over which κ is measured (Ktenidou et al. 2014); however, we relax this criterion to an SNR of 2 due to the higher noise level of the QCN sensors as was shown to be permissible based on the analysis of 12-bit QCN sensors by Neighbors et al. (2015). Note that the original records have been corrected for expected site response using amplification factors of Kaiser et al. (2016) and Oth and Kaiser (2014) (see Sect. 3); thus, we consider the κ measured here to be a "residual κ," κ_r, or any path and site attenuation that was not accounted for in the site spectral correction. Moving forward, we will denote the residual κ measured by the Anderson and Hough method as $\kappa_{AH,r}$, which is used as the initial best guess value in the forward modeling routine, and the residual κ_r fit to the spectra through the forward modeling routine as $\kappa_{SF,r}$.

With initial parameter values set, we then solve the forward model for a single M_0 and f_c per event, while inputting unique $\kappa_{AH,r}$ values per station-event record, across the frequency band 0.6 Hz $- f_x$ Hz, where f_x is the frequency limit determined to be unaffected by noise (i.e., SNR $\geq$2, the upper limit of $\kappa_{\mathrm{AH,r}}$ measurement). For the first iteration of the forward model, we calculate the squared residual between the data and the model. The partial first derivatives of this residual function constitute the Jacobian matrix that, assuming that the initial parameter values are suitably close to the true parameter value, allow convergence on the optimal spectral values through minimization of the residual function.

5. *Methods: Using the Gauss–Newton Optimization Method to Determine Spectral Parameters*

Following the first iteration of the forward model, we employ a simplification of the Newton method, i.e., the Gauss–Newton method, to minimize the residual squared function (e.g., Deuflhard 2004). The Gauss–Newton method is well suited for solving nonlinear least-squares problems, such as parametric regressions (e.g., Sheen et al. 2006; Alpak et al. 2011; Deuflhard 2004), and, thus, could conceivably be used to solve the parameters of the Brune spectral model as Eq. 2 is nonlinear with respect to seismic moment M_0 and corner frequency f_c (e.g., Drouet et al. 2010). The Gauss–Newton method is a modification of the more general Newton's method; however, in contrast to Newton's method second derivatives are not required so as to be computationally efficient (e.g., Loke and Dahlin 2002). As a gradient descent method, iterations move in the downhill direction to minimize a given function. Here, we minimize the residual squared function through a parameterization of M_0, f_0, and κ_{r} in Eq. 2 and obtain the Gauss–Newton iteration formula by expanding our squared residual function $f(\mathbf{B}) = \sum r(\boldsymbol{B})_i^2$ around $\mathbf{B}_n$, where $\mathbf{B}_n$ contains the variables M_0, f_c, and κ. Using a 3-D Taylor series, we have

$$f(\boldsymbol{B_n} + \Delta\boldsymbol{B}) = f(\boldsymbol{B_n}) + \left(\frac{\partial f}{\partial M_0}, \frac{\partial f}{\partial f_c}, \frac{\partial f}{\partial \kappa_r}\right)\begin{pmatrix}\Delta M_0\\ \Delta f_c\\ \Delta \kappa_r\end{pmatrix}$$

$$+\frac{1}{2}(\Delta M_0, \quad \Delta f_c, \quad \Delta\kappa)\begin{bmatrix}\frac{\partial^2 f}{\partial M_0^2} & \frac{\partial^2 f}{\partial M_0 \partial f_c} & \frac{\partial^2 f}{\partial M_0 \partial \kappa_r}\\ \frac{\partial^2 f}{\partial M_0 \partial f_c} & \frac{\partial^2 f}{\partial f_c^2} & \frac{\partial^2 f}{\partial f_c \partial \kappa_r}\\ \frac{\partial^2 f}{\partial M_0 \partial \kappa_r} & \frac{\partial^2 f}{\partial f_c \partial \kappa_r} & \frac{\partial^2 f}{\partial \kappa_r^2}\end{bmatrix}\begin{pmatrix}\Delta M_0\\ \Delta f_c\\ \Delta \kappa_r\end{pmatrix} + \cdots \tag{5}$$

Note that f is describing a general function and $\Delta\boldsymbol{B}$ is assumed to be small. Truncating the function at the quadratic term, we obtain

$$f(\boldsymbol{B_n} + \Delta\boldsymbol{B}) \approx f(\boldsymbol{B_n}) + \boldsymbol{g}_n^{\mathrm{T}}\Delta\boldsymbol{B} + \frac{1}{2}\Delta\boldsymbol{B}^{\mathrm{T}}\boldsymbol{H}_n\Delta\boldsymbol{B}, \tag{6}$$

where $\mathbf{g}_n$ is the gradient vector with respect to M_0, f_c, and κ_r and $\mathbf{H}_n$ is the Hessian matrix with respect to M_0, f_c, and κ_{r}. To determine the minimum of the above perturbation equation, we set the gradient [with respect to perturbations $\Delta\boldsymbol{B}$, i.e., the transpose of the gradient of f is $(\frac{\partial f}{\partial \Delta M_0}, \frac{\partial f}{\partial \Delta f_c}, \frac{\partial f}{\partial \Delta \kappa_r})$] equal to zero such that

$$\nabla f = \boldsymbol{g}_n + \boldsymbol{H}_n\Delta\boldsymbol{B} = 0, \tag{7}$$

with the corresponding solution

$$\Delta\boldsymbol{B} = -\boldsymbol{H}_n^{-1}\boldsymbol{g}_n. \tag{8}$$

Now, when we update $\boldsymbol{B}$ with each iteration of the forward model, we have

$$\boldsymbol{B_{n+1}} = \boldsymbol{B_n} + \Delta\boldsymbol{B} = \boldsymbol{B_n} - \boldsymbol{H}_n^{-1}\boldsymbol{g}_n \tag{9}$$

The Jacobian matrix is composed of derivatives at every frequency data point, f_i, where each column of the Jacobian matrix contains the derivative of the residual function with respect to one of the three variables (M_0, f_c, κ_{r}). For our purposes, the Jacobian matrix is a three column matrix with imax number of rows, where each row represents the derivative of the residual, r, evaluated at each sample frequency point (f_i). It appears as:

$$\boldsymbol{J} = \begin{bmatrix}\frac{\delta r_1}{\delta M_0} & \frac{\delta r_1}{\delta f_c} & \frac{\delta r_1}{\delta \kappa_{\mathrm{r}}}\\ \frac{\delta r_2}{\delta M_0} & \frac{\delta r_2}{\delta f_c} & \frac{\delta r_2}{\delta \kappa_{\mathrm{r}}}\\ \vdots & & \\ \frac{\delta r_{\mathrm{imax}}}{\delta M_0} & \frac{\delta r_{\mathrm{imax}}}{\delta f_c} & \frac{\delta r_{\mathrm{imax}}}{\delta \kappa_{\mathrm{r}}}\end{bmatrix}, \tag{10}$$

where $\boldsymbol{J}$ is the Jacobian matrix and r_i is the residual for each frequency f_i up to the last frequency point, f_{imax}. The residual misfit is obtained by subtracting the model from the data for each f_{i} and determining the first derivative of the residual function to direct the subsequent best guess for each of the three variables. We note that taking the derivative of the residual squared function leads to

$$\frac{\partial}{\partial B_k}\sum_{1}^{\text{imax}} r_i^2 = \sum_{1}^{\text{imax}} 2r_i \frac{\partial r_i}{\partial B_k}, \tag{11}$$

with B_k being either M_0, f_{c}, or κ_r. Thus, Eq. 11 gives the following relationship:

$$\boldsymbol{g}_n = 2\boldsymbol{J}^{\text{T}}\boldsymbol{r}. \tag{12}$$

Taking the second derivative of the residual squared function leads to a relation with the Hessian matrix

$$\begin{aligned}\frac{\partial^2}{\partial B_l \partial B_k}\sum_{1}^{\text{imax}} r_i^2 &= 2\frac{\partial}{\partial B_l}\sum_{1}^{\text{imax}} r_i \frac{\partial r_i}{\partial B_k} \\ &= 2\sum_{1}^{\text{imax}} \frac{\partial r_i}{\partial B_l}\frac{\partial r_i}{\partial B_k} + 2\sum_{1}^{\text{imax}} r_i \frac{\partial^2 r_i}{\partial B_l \partial B_k},\end{aligned} \tag{13}$$

so that

$$\mathbf{H}_{\boldsymbol{n}} = 2\boldsymbol{J}^{\text{T}}\boldsymbol{J} + 2\sum_{1}^{\text{imax}} r_i \frac{\partial^2 r_i}{\partial B_l \partial B_k}. \tag{14}$$

Since the second term on the right in Eq. 14 is multiplied by the residual r_i, then for small residual values we have

$$\mathbf{H}_{\boldsymbol{n}} \approx 2\boldsymbol{J}^{\text{T}}\boldsymbol{J}. \tag{15}$$

Finally, the Gauss–Newton iterative formula (substituting Eqs. 12 and 15 into Eq. 9) can be written as:

$$\boldsymbol{B}_{\boldsymbol{n}+1} = \boldsymbol{B}_{\boldsymbol{n}} - \left(\boldsymbol{J}^{\text{T}}\boldsymbol{J}\right)^{-1}\boldsymbol{J}^{\text{T}}\boldsymbol{r}_{\boldsymbol{n}}, \tag{16}$$

where $\boldsymbol{B}_{\boldsymbol{n}}$ is an array of the best guess initial parameters or subsequent iteration parameters while $\boldsymbol{B}_{\boldsymbol{n}+1}$ is the new solution of parameters that is perturbed, presumably in the correct direction, from previous solution parameters. $\boldsymbol{r}_{\boldsymbol{n}}$ is the array of residual misfits for each f_i. This procedure is repeated until stabilization of the parameters occurs (difference of less than 1×10^{-4} Hz and 1×10^{-5} s for subsequent iterations of trial values of f_{c} and κ_r respectively), which is typically achieved in fewer than ten iterations.

We note that the Gauss–Newton method has some limitations; for instance, problems can arise if $\boldsymbol{J}^{\text{T}}\boldsymbol{J}$ is near singular or ill conditioned (i.e., very small eigenvalues). Additionally, convergence to the correct values is not guaranteed; an initial guess that is far from the global minimum may focus on a local minimum or fail to converge entirely. We check for physically realistic results by visually inspecting the model fits to the data (Fig. 4) and verifying that the best-fit moment magnitude, $M_{\text{w,SF}}$ (where SF indicates spectral fit), correlates well with the $M_{\text{w,GNS}}$. However, it is more difficult to visually assess the accuracy of the f_{c} solution; this is particularly a concern given that the Brune spectral model can be biased by strong high-frequency attenuation (i.e., κ). As a proxy check on f_{c}, we consider the variation in best guess initial $\kappa_{\text{AH,r}}$ and resultant $\kappa_{\text{SF,r}}$ values to detect potential strong tradeoffs with the f_{c}. If κ_r remains approximately constant in value before and after the fitting procedure (i.e., there is little difference in value between $\kappa_{\text{AH,r}}$ and $\kappa_{\text{SF,r}}$), we assume that f_{c} was not influenced by fluctuations in $\kappa_{\text{SF,r}}$ during the iterative forward modeling procedure and is, therefore, robust.

Following these quality checks, we use the optimal source parameter solutions to calculate the stress drop assuming a circular fault of radius, R, and the conventional constants (Brune 1970, 1971) as

$$R = \left(\frac{2.34\times\beta}{2\times\pi\times f_c}\right), \tag{17}$$

where the corner frequency, f_{c}, is obtained from the spectral fitting procedure. The f_{c} of the spectrum is assumed to be inversely proportional to the source duration and, therefore, correlated to fault dimension and the stress drop by Eshelby (1957)

$$\Delta\sigma = \left(\frac{7M_0}{16R^3}\right), \tag{18}$$

where $\Delta\sigma$ is interpreted to relate the slip to the fault dimension. Among other assumptions, the adoption

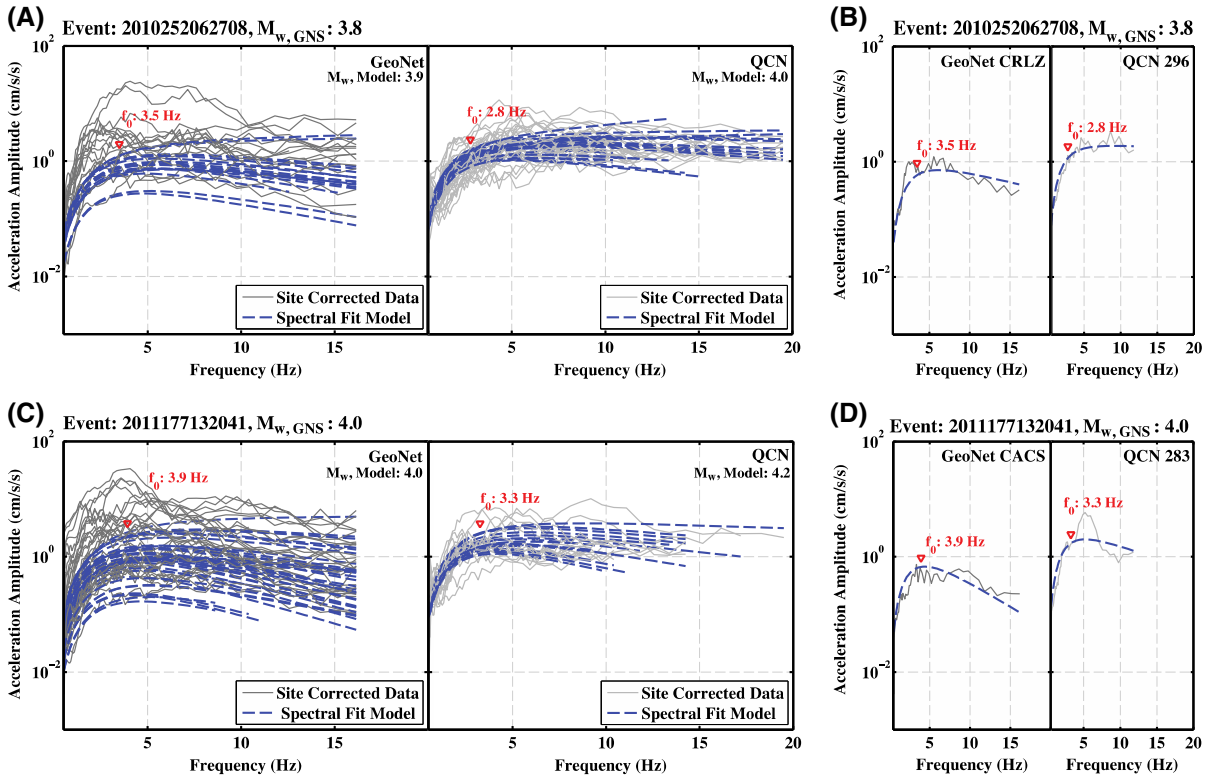

Figure 4

Plots of site corrected acceleration spectra for **a** $M_{W,GNS}$ 3.8 and **c** $M_{W,GNS}$ 4.0 with the range of site corrected, smoothed GeoNet and QCN data shown by *gray shading*. The spectral model results for each station are plotted as *blue dashed lines*; note that one f_c and M_0 are determined for all horizontal records that captured the event while κ varies per station record. Best fitting f_c and M_w solutions for each network are marked on the respective plots. For clarity, **b**, **d** show examples of individual event-station spectral fit results for nearby (<5 km) QCN and GeoNet stations shown in **a**, **c**, respectively

of a single shear wave velocity, β, as is done here can affect $\Delta\sigma$ uncertainty, as β has a cubic relationship with stress drop. We justify this prescription as the majority of the events occur within a relatively shallow range of hypocentral depths between 5 and 10 km with a median of 8 km. Similarly, the underlying assumption of frequency-independent κ attenuation may be problematic, especially considering that Kaiser et al. (2016) observe both lower frequency amplification potentially due to deeper Christchurch basin wave effects as well as higher frequency site effects in the range of 4–6 Hz that they attribute to shallow sediment and water table layers in the near surface. However, these frequency-dependent effects should be largely accounted for by the Kaiser et al. (2016) site response functions and overall the corrected source spectra appear to be well described by the source model (e.g., Fig. 4).

6. Results: Moment Magnitude, $M_{w,SF}$

We performed spectral forward modeling for 139 events of the Canterbury aftershock sequence, ranging in magnitude from $3.6 \geq M_w \leq 5.6$. We apply the Gauss–Newton method to obtain the seismic moment, M_0, with which we calculate the moment magnitudes for these events. Figure 5 shows the resulting spectral fits plotted relative to the GNS catalog magnitudes. We find that the $M_{w,SF}$ estimates are consistent with $M_{w,GNS}$, with a median absolute difference of 0.09 and 0.17 for GeoNet and QCN station data, respectively. We also perform the spectral modeling on aftershocks that were recorded by both networks; combining GeoNet and QCN records for these events, we find a median difference of 0.11 between $M_{w,SF}$ estimates and the catalog $M_{w,GNS}$ (Fig. 5). Overall, the GeoNet $M_{w,SF}$ results

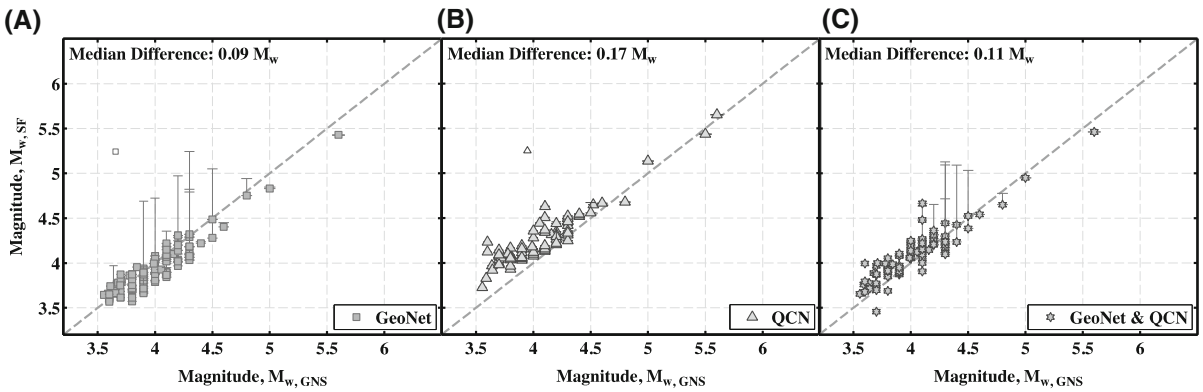

Figure 5
Plots of GNS catalog magnitude ($M_{W,GNS}$) versus corresponding event magnitude from the spectral fitting routine ($M_{W,SF}$), where **a** shows results for GeoNet records, **b** QCN records, and **c** combined GeoNet and QCN records. In (**c**), we only consider events recorded by stations in both networks. *Dashed gray line* shows one-to-one relationship for reference. *Error bars* depict the lower 20th and upper 80th percentile of $M_{W,SF}$

cluster along the 1:1 reference line with the $M_{w,GNS}$ catalog; spectral fits based on QCN records produce a similar pattern, though with a higher overall misfit. We identify several outliers that have a difference in magnitude ($M_{w,SF}$ compared to $M_{w,GNS}$) greater than or equal to 1; these events are shown in the panels of Fig. 5, but are removed from later analysis procedures. In general, outlier solutions may suffer from poorer quality or a fewer number of recordings, ill-defined initial conditions for the parametric approach, or, more likely, a complex residual function with local minima near the global minimum, or the 'true' parameter value. The local minima trap is a well-recognized pitfall in optimization problems and emphasizes the practice of employing good initial parameter estimates.

As solutions of downhill optimization procedures can be dependent on the choice of initial condition, we estimate the uncertainty in the $M_{w,SF}$ results by considering the sensitivity of the results to the initial parameter value. Taking 10 trial M_0 values logarithmically spaced in the range of ± 0.5 units from the best guess initial $M_{w,GNS}$, we re-fit the data and examine the variation in the $M_{W,SF}$ results. Error bars in Fig. 5 represent the lower 20th and upper 80th percentile of the $M_{w,SF}$ results, in effect a measure of statistical distribution for which 20% of the resulting spectral fit results are larger and 80% are smaller, for each event. Additionally, for all events we calculate the mean of the difference between each of the 10 trial values for the initial M_w and the final $M_{w,SF}$ determined using the best guess initial M_w. We find that the mean of the differences is 9.72×10^{-2}, 2.27×10^{-2}, 6.23×10^{-2}, for GeoNet, QCN, and combined networks, respectively, indicating that the $M_{w,SF}$ results are not strongly dependent on the initial parameter value. However, we observe for a small number of events that as the trial value of the initial $M_{w,SF}$ is increased the final $M_{w,SF}$ tends to also increase; this can be seen for some events in Fig. 5, where the error bars for the 80th percentile are larger than those of the 20th percentile.

7. Results: Resolving $\kappa_{AH,r}$ and $\kappa_{SF,r}$

For the non-linear Brune model, a well-defined initial estimate for the high-frequency attenuation, κ, is particularly crucial as the shape of the spectra at high frequencies can systematically influence the determination of the source parameters. Thus, we graphically fit each spectral record prior to the forward modeling, solving for a so-called residual $\kappa_{AH,r}$, a site corrected high-frequency attenuation estimate, to define the initial value and also to monitor the variation in the residual $\kappa_{SF,r}$ following the modeling procedure. In Fig. 6, we plot the range of κ values considered in this study, including (1) for reference, a κ measured off the raw spectrum using the Anderson and Hough (1984) method, called κ_{AH}, (2) an initial

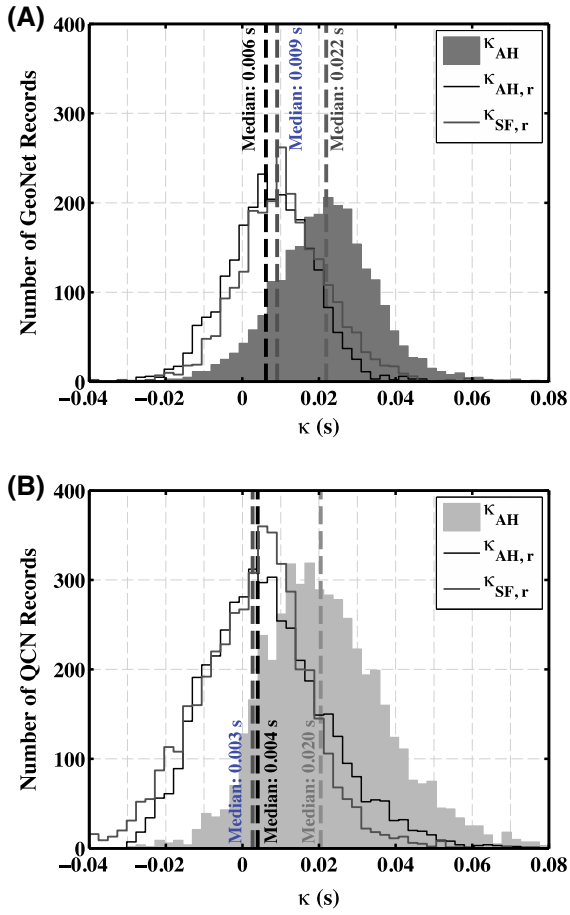

Figure 6
Histograms of κ values measured on **a** GeoNet station records and **b** QCN records. Three κ values were considered in this study: (1) an Anderson and Hough (1984) κ value (denoted κ_{AH} for Anderson and Hough) shown in *solid gray*, (2) a residual κ measured on the site corrected spectra using the Anderson and Hough method, $\kappa_{AH,r}$, shown as a *black line* and (3) a residual κ fit in the Gauss–Newton spectral modeling procedure, $\kappa_{SF,r}$, shown as a *blue line*. The median values of κ_{AH}, $\kappa_{AH,r}$, and $\kappa_{SF,r}$ are shown by a *dashed line* of their *respective colors*

residual κ fit to the site corrected spectrum using the Anderson and Hough (1984) method, $\kappa_{AH,r}$, and (3) a residual κ fit during the spectral model, $\kappa_{SF,r}$. κ_{AH} gives some indication of the strength and distribution of the high-frequency attenuation values for the region; here, we find similar median κ_{AH} values of 0.022 and 0.020 s for GeoNet and QCN station data, respectively. We observe that QCN records have a greater number of records with large κ_{AH} values (e.g., >0.04 s), which may be expected considering the Christchurch locales where QCN stations were installed including many of the neighborhoods that experienced high amplification.

Comparing κ_{AH} and $\kappa_{AH,r}$ gives an indication of the effect of the applied site correction at high frequencies. We see that the site corrections act to decrease the spectral decay and "flatten" the high-frequency portion of the spectra. The site-specific correction decreases the median κ value by 0.016 s for GeoNet records and the generic site correction lowers the median κ value by 0.016 s for QCN data. Though the site corrections only approach the high-frequency plateau of the Brune model, it is not critical for the site correction to completely flatten the spectrum (i.e., $\kappa = 0$). Rather, the main purpose of the site correction is to decrease the relatively low-frequency basin-trapped wave amplification, which affects the source parameter estimates, and to provide an accurate estimation of κ_r in Eq. (1) to calculate the "true" f_c. Thus, the $\kappa_{AH,r}$ here only serves to quantify the high-frequency decay following the site correction. For GeoNet records, we find a median initial $\kappa_{AH,r}$ to be 0.006 s and a final median $\kappa_{SF,r}$ to be 0.009 s, while QCN records have a median initial $\kappa_{AH,r}$ of 0.004 s and a final $\kappa_{SF,r}$ of 0.003 s. For both networks, the difference in the median $\kappa_{AH,r}$ and $\kappa_{SF,r}$ is small, particularly in the context of the range of κ values measured. With relatively little movement between the initial $\kappa_{AH,r}$ and final $\kappa_{SF,r}$ values, we are confident that limited to no tradeoff occurs between $\kappa_{SF,r}$ and source parameters, namely f_c, during the spectral model; thus, we conclude that the fitted f_c can be reliably used to estimate the stress drops.

8. Results: Stress Drop, $\Delta\sigma$

In Fig. 7, we plot the moment magnitude obtained from the spectral fitting procedure against the fitted corner frequency for each event with lines of constant stress drop overlain for reference. As done with the $M_{w,SF}$ results, we investigate the dependence on the best guess initial f_c parameter by testing a set of ten trial initial f_c values logarithmically spaced across $f_c \times (10^{\pm 0.5})$ Hz of the initial corner frequency. The variation in the $f_{c,SF}$ results produced by the 10 trial initial f_c values compared to $f_{c,SF}$ determined using the best guess initial f_c was extremely small. The

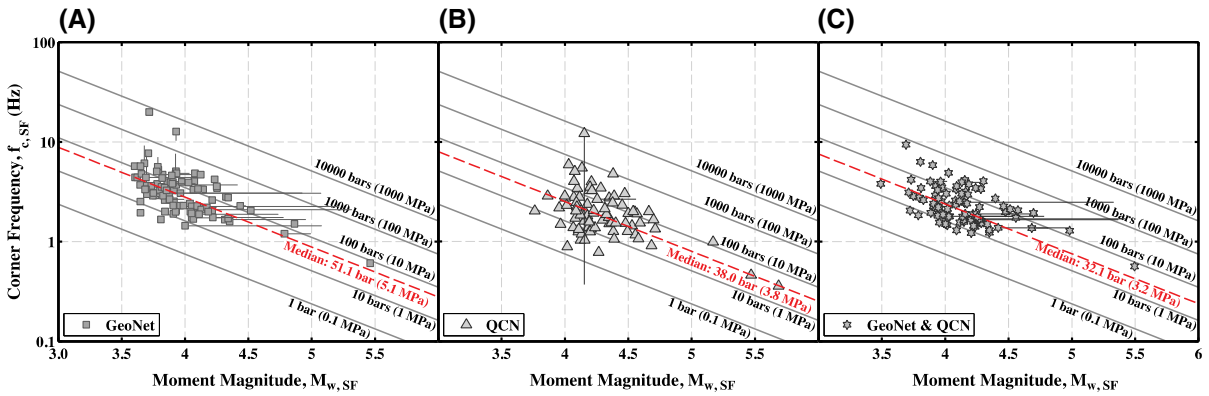

Figure 7

Plot of f_c vs. M_w obtained from spectral fitting routine, where **a** shows fits for GeoNet records alone, **b** QCN records, and **c** combined GeoNet and QCN for station data. *Lines* of constant stress drop are plotted for reference (*solid gray*) as well as the median stress drop for each dataset (*dashed red*). *Error bars* depict the lower 20th and upper 80th percentile of $M_{w,SF}$ and $f_{c,SF}$ estimates. Events with apparently no error bars have only small variations between the "best guess"-based estimates and the 20th and 80th percentile and thus *error bars* are overlapped by the event symbol

mean of the differences is 1.06×10^{-1}, 4.76×10^{-2}, and 1.89×10^{-2} for GeoNet, QCN, and combined networks, respectively. Thus, the $f_{c,SF}$ determined is largely independent of the initial f_c chosen.

Inserting the calculated f_c into Eqs. (17) and (18), we calculate the stress drop for the events based on GeoNet data, QCN data, and combined GeoNet and QCN network records. We obtain a median stress drop of 5.11 and 3.80 MPa for events records from only GeoNet or QCN stations, respectively, and 3.21 MPa for the spectra from both networks (Fig. 7). The stress drop estimates cluster between 1 and 100 MPa, though the majority of events exhibit stress drops between 1.7 and 13.0 MPa based on 20th and 80th percentiles of the combined network results. These estimates are well within the range of 1–20 MPa, with a median value of 5 MPa, previously determined by Oth and Kaiser (2014) using a non-parametric approach applied to GeoNet station records within the greater Christchurch region (Fig. 8).

For the combined networks, the stress drops range from 0.7 to 67 MPa and appear to have a similar distribution as the stress drops determined by Oth and Kaiser (2014). We examine whether the stress drops are observed to vary with depth, magnitude, and/or if there are lateral variations across the sequence. We find no apparent correlation between stress drop and event size (i.e., $M_{w,SF}$) nor depth (Fig. 9). Figure 9a shows the mapped distribution of stress drops for this catalog. Clusters of higher stress drops exist at the eastern edge of 2010 Darfield mainshock rupture on the Greendale fault. Higher stress drops are observed for events that occur along the eastern portion of the 2011 M_w 6.2 Christchurch rupture and western extent of the 2011 M_w 6.0 event. In contrast, aftershocks that occur along the western portion of the M 6.2 Christchurch rupture have lower-than-average stress drops. The observed lateral variation in stress drops closely mirrors the variations highlighted by Oth and Kaiser (2014). Though we have limited temporal extent in stress drop (Fig. 9b), we note that events associated with the 2011 M_w 6.2 and M_w 6.0 events have higher stress drops than those immediately following the Darfield mainshock (Fig. 9d).

9. Discussion

Previous studies have identified methods to estimate Brune model parameters (e.g., Anderson and Humphrey 1991; Abercrombie 1995; Hough 1997; Edwards et al. 2010; Oth et al. 2011); here, we show that a non-linear least-squares Gauss–Newton method can provide accurate source estimations. The spectral fits produce $M_{w,SF}$ that are similar to the catalog magnitudes ($M_{w,GNS}$), with a median difference of 0.11. We show that the Gauss–Newton method

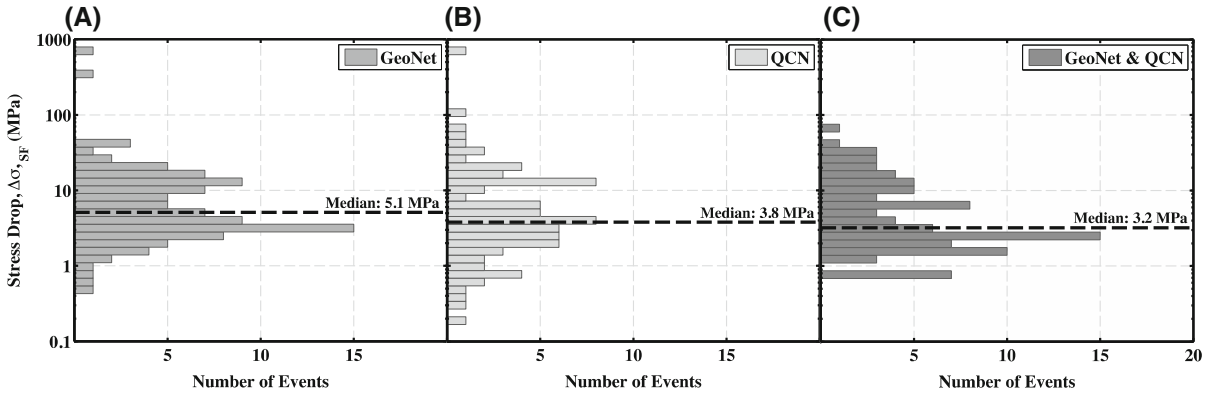

Figure 8
Plots of stress drop results; **a** shows the stress drop distribution and median stress drop of 5.1 MPa for GeoNet data, **b** displays the stress drop distribution and median stress drop of 3.8 MPa for QCN data, and **c** shows the stress drop distribution and median stress drop of 3.2 MPa for combined GeoNet and QCN records. While the stress drops range from 0.7 to 67 MPa for the combined networks

produces consistent results over a range of trial initial values for M_0 (i.e., within ± 0.5 of the $M_{w,GNS}$) and f_c (± 5 Hz of the theoretical f_c on a logarithmic scale). Trial values of the initial M_0 and f_c values produce nearly identical results to those obtained using the best guess initial parameter values, with a mean difference for the combined networks of 1.89×10^{-2} for $f_{c,SF}$ and 6.23×10^{-2} for $M_{w,SF}$. Thus, we conclude that our results are not strongly dependent on the initial values chosen.

We minimize the potential tradeoff between κ and the source parameters (i.e., corner frequency) in the model by taking into account the local site effects. Specifically, we divide the raw spectra by the station- and geology-dependent amplification factors from Kaiser et al. (2016) and Oth and Kaiser (2014), which remove or at least reduce the influence of local site geology on the spectra. Application of the site-specific amplification corrections in particular resulted in good fits for the GeoNet stations by accounting for the low-frequency basin-trapped wave energy, as also seen for the dataset in Oth and Kaiser (2014), although note that an additional frequency-dependent path correction is applied to source spectra in that study. Accounting for path and site effects is particularly crucial in a region like Christchurch, where basin path effects and strong, highly variable site response due to shallow aquifer layers dominate the spectra. We find a median $\kappa_{SF,r}$ of 0.006 and 0.004 s for the GeoNet and QCN stations, respectively, which are smaller than the median raw κ_{AH} estimates of 0.022 and 0.020 s. While any residual κ indicates that some path and site attenuation still affect the high-frequency portion of the spectrum, both site-specific and generic site corrections have reduced this effect. We infer that our method could also successfully be applied using site-specific amplification curves determined through simpler independent methods (e.g., site-to-reference spectral ratios) to improve source spectral fits.

By properly accounting for κ, it is possible to limit the potential underestimation of f_c during the spectral fitting process. However, there may be some concern that the initial best guess $\kappa_{AH,r}$ measurements may contain bias from the source; therefore, one benefit of simultaneous spectral modeling for both f_c and $\kappa_{SF,r}$ is to find the parameters that best match the overall shape of the spectra. We conclude that, based on the stability of both the final $\kappa_{SF,r}$ and $f_{c,SF}$, even for a wide range of trial initial f_c, there is minimal tradeoff between these values. Additionally, if $\kappa_{SF,r}$ were influencing $f_{c,SF}$ we would expect to see a correlation between stress drops (derived from $f_{c,SF}$) and magnitude, such that smaller magnitude events would have lower stress drops (due to lower $f_{c,SF}$) for smaller magnitude events (i.e., Anderson 1986). However, we observe no such trend between stress drop and magnitude.

We use $M_{w,SF}$ and $f_{c,SF}$ to estimate stress drops for the Canterbury sequence and find median stress drops

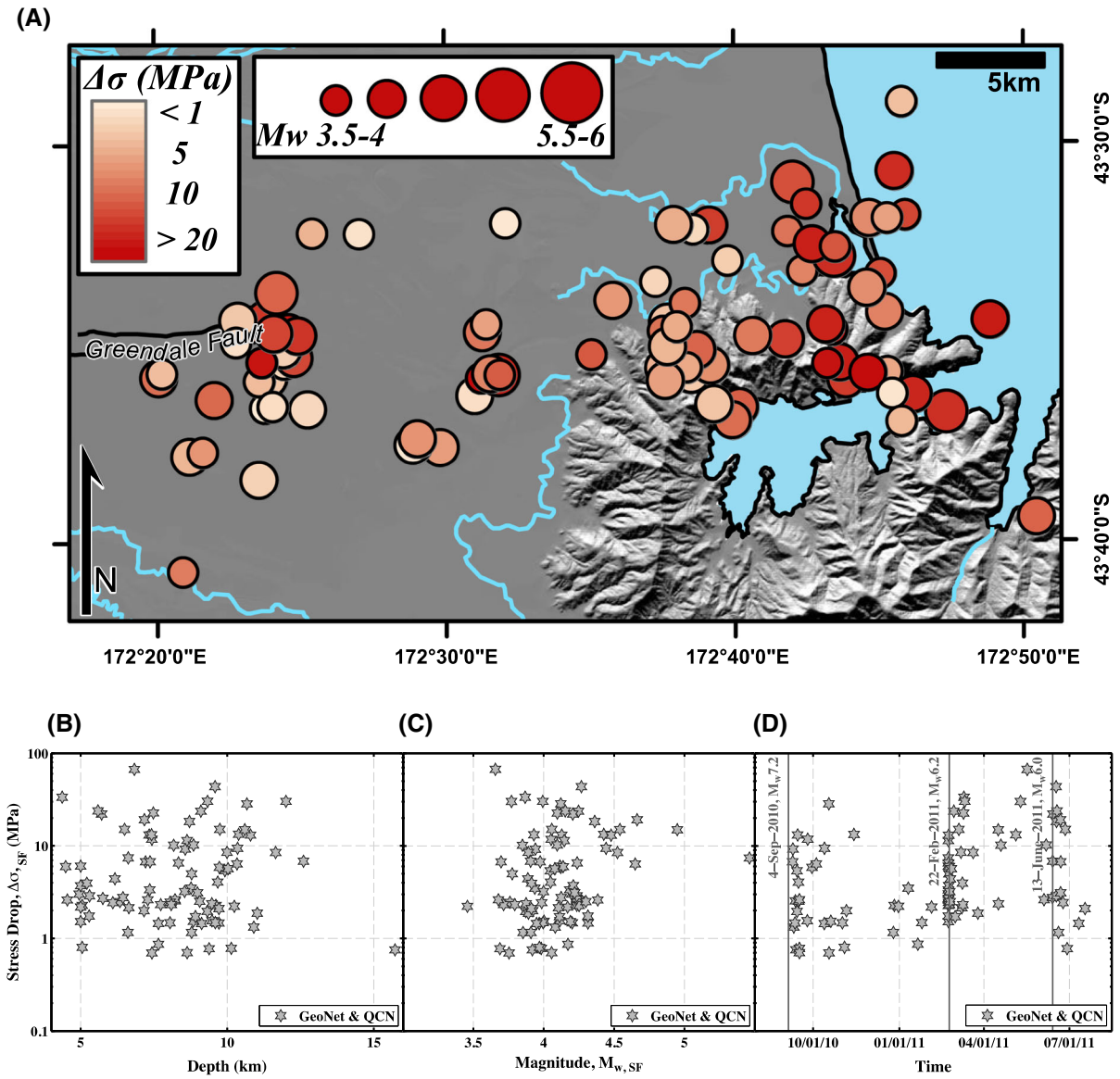

Figure 9

a Map of stress drop results, where *brighter red* indicates higher stress drop. *Symbols* are scaled by $M_{w,SF}$ results. The relationships between stress drop and depth and stress drop and $M_{W,SF}$ are shown in **b**, **c**, respectively. **d** Stress drop plotted in time with the three largest events of the sequence plotted for reference

of 5.1 and 3.8 MPa, for GeoNet and QCN data, respectively, and 3.2 MPa when data are combined. These stress drops are consistent with other studies in the region, namely Oth and Kaiser (2014), who used a non-parametric spectral inversion to separate source spectra and frequency-dependent site and path terms (e.g., Castro et al. 1990; Oth et al. 2011) and report a median stress drop of 5 MPa. Our reported stress drops fall in the typical range reported in global studies of stress drops (0.1–50 MPa) (e.g., Kanamori and Anderson 1975; Choy and Boatwright 1995; Allmann and Shearer 2009). However, the stress drops are somewhat higher than typically found for tectonically active settings; for example, Kanamori and Anderson (1975) report average stress drops of 3 MPa for interplate events and Oth et al. (2010) report median stress drops of 1 MPa for events in Japan. Higher overall stress drops are often reported

for intraplate regions compared to interplate regions (e.g., Kanamori and Anderson 1975; Zhou and Kanamori 1987; Choy and Boatwright 1995). It has been posited that stress drops are higher for the Canterbury sequence as it occurs in a low seismicity intraplate region with likely well-healed, immature faults (e.g., Fry and Gerstenberger 2011; Oth and Kaiser 2014).

The reported stress drops range from 0.7 to 67 MPa, with the majority of events having stress drops between 1.7 and 13.0 MPa (20th and 80th percentile, correspondingly) for the combined networks. Most of the stress drops fall within approximately one order of magnitude variability, though it is not uncommon to observe large variability in stress drops, particularly for large datasets; for example, Oth et al. (2010) and Baltay et al. (2011) report stress drops in Japan ranging from 0.1 to 100 MPa and Allmann and Shearer (2009) similarly show large variability in global estimates. The stress drops and their overall variability that we report are nearly identical to those reported in Oth and Kaiser (2014) who find stress drops between 1 and 20 MPa. As noted in Oth and Kaiser (2014), this may suggest that the local variability in stress drops is lower for individual sequences. Indeed, we find clear clustering of high and low stress drops even within the Canterbury sequence, which is discussed in more detail below.

We observe that stress drops vary spatially across the Canterbury sequence, with distinct clustering of higher and lower stress drops. We find higher than average stress drops concentrated along the eastern side of the Greendale fault. Similarly, higher stress drop events also seem to cluster near the coastline where the eastern-most events in the sequence occur. In contrast, low stress drop events seem to cluster along the westernmost portion of the M_w 6.2 Christchurch earthquake rupture. The spatial distribution of stress drops that we report here is very similar to the distribution found by Oth and Kaiser (2014). It is known that stress drops can vary with source mechanism (e.g., Allmann and Shearer 2009); the Canterbury sequence contains a mix of source mechanisms, but there does not appear to be a clear clustering of a specific mechanism type in the areas of higher or lower stress drops (Sibson et al. 2011). Oth and Kaiser (2014) note that higher stress drops are observed at the rupture edges and suggest that they may be due to local stress concentrations resulting from the ruptures themselves. If this is correct we might expect to see stress drops reduce with time as stress concentrations are relieved; while we do not have sufficient temporal coverage to look for such trends, we do note that the M_w 6.2 and M_w 6.0 appear to have larger stress drops than the aftershocks immediately following the Darfield mainshock. Given the large number of possible controls on stress drop, e.g., geologic material, presence of fluids, etc., it is difficult to posit what may be controlling the spatial variation in stress drops that we observe.

Of interest in this study is the performance of the QCN sensors in deriving spectral source parameters. Lawrence et al. (2014) and Chung et al. (2015) show that the lower resolution acceleration time series can be used to estimate magnitudes and Neighbors et al. (2015) show that high-frequency spectral data can be used to characterize the κ_{AH} site parameter; however, the determination of low-frequency source parameters, such as moment, has not previously been assessed using local earthquake records. A benefit of a larger number of stations used in source parameter studies is that an extensive network can effectively average out directivity effects when good azimuthal coverage is achieved. Here, we show that we can recover reliable estimates of the seismic moment from the low-frequency spectra, and the corresponding moment magnitude. The median difference between $M_{w,SF}$ using only QCN data compared to the GNS catalog magnitude ($M_{w,GNS}$) is 0.17 compared to 0.09 when using only GeoNet data. The variability of stress drops estimated with only QCN data is somewhat larger than for GeoNet only data. This difference could be attributed to the lower resolution of the sensors resulting in overall lower SNR levels and/or differences in their installation (e.g., coupling, building response). The use of generic geologic site corrections for the temporary QCN RAMP deployment, rather than site-specific site correction used for GeoNet stations, may also explain the larger median moment magnitude difference. In other words, spectral amplification from residual path and site effects could conceivably create an overestimation bias in

M_0. Overall, we find that we recover similar source and site parameters for QCN data compared to traditional accelerometer data. Based on these results, we believe that it is appropriate to integrate MEMS data with higher-resolution network data for seismic parameter estimations, particularly where available higher-resolution network data are limited.

10. Conclusion

We confirm the use of the Gauss–Newton method for use in Brune spectral problems to derive source parameters and kappa for a subset of events in the Canterbury sequence ranging from $3.6 \leq M_w \leq 5.6$. The catalog considered here covers corner frequency values that span an order of magnitude and, that we can accurately recover the corner frequency and kappa, indicates this method is not strongly affected by tradeoffs between corner frequency and attenuation. We are able to recover the catalog $M_{w,GNS}$ with a median difference of 0.09 with 24-bit GeoNet accelerometers after applying a site-specific amplification correction. Using lower-resolution, 14-bit QCN MEMS accelerometers and applying a generic geology-based amplification correction, we are able to match the catalog $M_{w,GNS}$ with a median difference of 0.17. This suggests that QCN sensors can be used to recover magnitudes using a low-frequency spectral approach.

We find median Brune stress drops of 5.1 and 3.80 MPa for GeoNet and QCN data, respectively. We observe a clear spatial clustering of the stress drops in the sequence, but there is no correlation between stress drop and depth or magnitude. As previously noted by Fry and Gerstenberger (2011) for apparent stress and Oth and Kaiser (2014) for static stress drop, we find that the Canterbury events have overall high stress drops consistent previous studies reporting higher stress drops for intraplate events.

Acknowledgements

We would like to thank all the volunteers who hosted sensors, without whom this research would not be possible. Additionally, we thank QCN team members, particularly Angela Chung and Carl Christensen, and the GNS team including students from Victoria University of Wellington for the quick deployment of the sensors and data capture. University of California, Riverside undergraduate student Eric Liao provided tremendous help in initial acquisition and visual inspection of the QCN data. Geologic data for New Zealand were graciously provided by David Heron from the GNS QMap group. We acknowledge the New Zealand GeoNet project and its sponsors EQC, GNS Science and LINZ, for providing seismic data used in this study and also the support of the New Zealand Natural Hazards Platform. We thank Stéphane Drouet, Dino Bindi, Adrien Oth, Sue Hough and Annemarie Baltay for constructive comments that improved the paper. Any use of trade, firm, or product names is for descriptive purposes only and does not imply endorsement by the U.S. Government.

References

Abercrombie, R. E. (1995). Earthquake source scaling relationships from −1 to 5 ML, using seismograms recorded at 2.5 km depth. *Journal of Geophysical Research, 100*, 24015–24036.

Abercrombie, R. E. (2015). Investigating uncertainties in empirical Green's function analysis of earthquake source parameters. *Journal of Geophysical Research Solid Earth, 120*, 4263–4277.

Allmann, B. P., & Shearer, P. M. (2009). Global variations of stress drop for moderate to large earthquakes. *Journal of Geophysical Research, 114*, B01310.

Alpak, F. O., Habashy, T. M., Abubakar, A., Torres-Verdin, C., & Sepehrnoori, K. (2011). A multiplicative regularized Gauss-Newton algorithm and its application to the joint inversion of induction logging and near-borehole pressure measurements. *Progress in Electromagnetics Research B, 29*, 105–138.

Anderson, J. G. (1986). Implication of attenuation for studies of earthquake source. In *Earthquake Source Mechanics, Geophysical Monograph* (Vol. 37, pp. 311–318), Washington D.C.: AGU.

Anderson, J. G., & Hough, S. E. (1984). A model for the shape of the Fourier amplitude spectrum of acceleration at high frequencies. *Bulletin of the Seismological Society of America, 74*(5), 1969–1993.

Anderson, J. G., & Humphrey, J. R, Jr. (1991). A least squares method for objective determination of earthquake source parameters. *Seismological Research Letters, 62*, 201–209.

Baltay, A., Ide, S., Prieto, G., & Beroza, G. (2011). Variability in earthquake stress drop and apparent stress. *Geophysical Research Letters, 38*, L06303.

Bannister, S., Bill, F., Reyners, M., Ristau, J., & Zhang, H. (2011). Fine-scale relocation of aftershocks of the 22 February Mw 6.2 Christchurch earthquake using double-difference tomography. *Bulletin of the Seismological Society of America, 82*(6), 839–845.

Benson, K., Schlachter, S., Estrada, T., Taufer, M., Lawrence, J., & Cochran, E. (2013). On the powerful use of simulations in the Quake-Catcher Network to efficiently position low-cost earthquake sensors. *Future Generation Computer Systems, 29*(8), 2128–2142.

Boatwright, J., Fletcher, J. B., & Fumal, T. E. (1991). A general inversion scheme for source, site, and propagation characteristics using multiply recorded sets of moderate-sized earthquakes. *Bulletin of the Seismological Society of America, 81*(5), 1754–1782.

Boore, D. M., & Boatwright, J. (1984). Average body-wave radiation coefficients. *Bulletin of the Seismological Society of America, 74*(5), 1615–1621.

Brune, J. N. (1970). Tectonic stress and the spectra of seismic shear waves from earthquakes. *Journal of Geophysical Research, 75*(26), 4997–5009.

Brune, J. N. (1971). Correction to "Tectonic stress and the spectra of seismic shear waves from earthquakes". *Journal of Geophysical Research, 76*, 5002.

Castro, R. R., Anderson, J. G., & Singh, S. K. (1990). Site response, attenuation and source spectra of S waves along the Guerrero, Mexico, subduction zone. *Bulletin of the Seismological Society of America, 80*, 1481–1503.

Chen, J., Kemna, A., & Hubbard, S. S. (2008). A comparison between Gauss–Newton and Markov-chain Monte Carlo-based methods for inverting spectral induced-polarization data for cole–cole parameters. *Geophysics, 73*(6), F247–F259.

Choy, G. L., & Boatwright, J. L. (1995). Global patterns of radiated seismic energy and apparent stress. *Journal of Geophysical Research, 100*(B9), 18205–18228.

Chung, A. I., Neighbors, C., Belmonte, A., Miller, M., Sepulveda, H. H., Christensen, C., Jakka, R. S., Cochran, E. S., & Lawrence, J. F. (2011). The quake-catcher network rapid aftershock mobilization project following the 2010 M8.8 Maule, Chile earthquake. *Seismological Research Letters, 82*(4), 526–532. doi:10.1785/gssrl.82.4.526.

Chung, A. I., Cochran, E. S., Kaiser, A. E., Christensen, C. M., Yildirim, B., Lawrence J. F. (2015). Improved rapid magnitude estimation for a community-based, low-cost MEMS accelerometer network. *Bulletin of the Seismological Society of America, 105*(3), 1314–1323.

Cochran, E. S., Lawrence, J. F., Christensen, C., & Jakka, R. S. (2009). The Quake-Catcher Network: Citizen science expanding seismic horizons. *Seismological Research Letters, 80*, 26–30.

Cochran, E. S., Lawrence, J. F., Kaiser, A., Fry, B., Chung, A., & Christensen, C. (2011). Comparison between low-cost and traditional MEMS accelerometers: A case study from the M7.1 Darfield, New Zealand, aftershock deployment. *Annals of Geophysics, 54*(6), 729–737.

Deuflhard, P. (2004). *Newton Method for Nonlinear Problems: Affine Invariance and Adaptive Algorithms* (pp. 1–432). Berlin, Heidelberg: Spring Series in Computational Mathematics, Springer.

Dominguez, L. A., Yildirim, B., Husker, A. L., Cochran, E. S., Christensen, C. M., Cruz-Atienza, V. M., & Lawrence, J. F. (2015). The Red Atrapa Sismos (Quake Catcher Network in Mexico): Assessing performance during large and damaging earthquakes. *Seismological Research Letters, 86*, 848–855.

Douglas, J., Gehl, P., Bonilla, L. F., & Gelis, C. (2010). A κ model for mainland France. *Pure and Applied Geophysics, 167*, 1303–1315.

Drouet, S., Cotton, F., & Guéguen, P. (2010). v_{S30}, κ, regional attenuation and M_w from accelerograms: application to magnitude 3-5 French earthquakes. *Geophysical Journal International, 182*, 880–898.

Edwards, B., Allmann, B., Fäh, D., & Clinton, J. (2010). Automatic computation of moment magnitudes for small earthquakes and the scaling of local to moment magnitude. *Geophysical Journal International, 183*, 407–420.

Eshelby, J. D. (1957). The determination of the elastic field of an ellipsoidal inclusion and related problems. *Proceedings of the Royal Society of London, A, 241*, 376–396.

Evans, J. R., Allen, R. M., Chung, A. I., Cochran, E. S., Guy, R., Hellweg, M., & Lawrence, J. F. (2014). Performance of several low-cost accelerometers. *Seismological Research Letters, 85*(1), 147–158.

Evans, J. R., Hamstra, R. H., Kündig, C., Camina, P., & Rogers, J. A. (2005). TREMOR: A wireless MEMS accelerograph for dense arrays. *Earthquake Spectra, 21*(1), 91–124.

Fernández, A. I., Castro, R. R., & Huerta, C. I. (2010). The spectral decay parameter kappa in northeastern Sonora, Mexico. *Bulletin of the Seismological Society of America, 100*, 196–206.

Fry, B., Benites, R., & Kaiser, A. (2011a). The character of accelerations in the Mw 6.2 Christchurch earthquake. *Seismological Research Letters, 82*(6), 846–852.

Fry, B., Benites, R. A., Reyners, M. E., Holden, C., Kaiser, A. E., Bannister, S. C., et al. (2011b). Strong shaking in recent New Zealand earthquakes. *Eos, 92*(41), 349–351.

Fry, B., Eberhart-Phillips, D., & Davey, F. J. (2014). Mantle accommodation of lithospheric shortening as seen by combined surface wave and teleseismic imaging in the South Island, New Zealand. *Geophysical Journal International, 199*(1), 499–513.

Fry, B., & Gerstenberger, M. C. (2011). Large apparent stresses from the Canterbury earthquakes of 2010 and 2011. *Seismological Research Letters, 82*, 833–838.

Gentili, S., & Franceschina, G. (2011). High frequency attenuation of shear waves in the southeastern Alps and northern Dinarides. *Geophysical Journal International, 185*, 1391–1416.

Gledhill, K., Ristau, J., Reyners, M., Fry, B., & Holden, C. (2011). The Darfield (Canterbury, New Zealand) Mw 7.1 earthquake of September 2010: A preliminary seismological report. *Seismological Research Letters, 82*(3), 378–386.

Hanks, T. C., & Kanamori, H. (1979). A moment magnitude scale. *Journal of Geophysical Research, 84*(B5), 2348–2350.

Hicks, G. J., & Pratt, R. G. (2001). Reflection waveform inversion using local descent methods: Estimating attenuation and velocity over a gas-sand deposit. *Geophysics, 66*(2), 598–612.

Hough, S. E. (1997). Empirical Green's function analysis: Taking the next step. *Journal of Geophysical Research, 102*(B3), 5369–5384.

Imanishi, K., Ellsworth, W. L., & Prejean, S. G. (2004). Earthquake source parameters determined by the SAFOD Pilot Hole seismic array. *Geophysical Research Letters, 31*, L12S09.

Kaiser, A. E., Benites, R. A., Haines, A. J., Chung, A. I., Cochran, E. S., & Fry, B. (2013). Using low-cost MEMS sensors to estimate site effects: case study from the Darfield earthquake aftershock QCN deployment. *New Zealand, Seismological Research Letters: Seismological Society of America Annual Meeting, Salt Lake City, UT, 84*(2), 387.

Kaiser, A., Holden, C., Beavan, J., Beetham, D., Benites, R., Celentano, A., et al. (2012). The Mw 6.2 Christchurch

earthquake of February 2011: preliminary report. *New Zealand Journal of Geology and Geophysics, 55*(1), 67–90.

Kaiser, A. E., Oth, A., Benites, R. A. (2016) Frequency-dependent attenuation and site amplification for Canterbury, New Zealand, from spectral inversion of ground motion data from the 2010–2011 earthquake sequence. In *5th IASPEI/IAEE international symposium: Effects of surface geology on seismic motion, Taipei Taiwan, August 15–17, 2016*.

Kanamori, H., & Anderson, D. L. (1975). Theoretical basis of some empirical relations in seismology. *Bulletin of the Seismological Society of America, 65*, 1073–1095.

Kilb, D., Biasi, G., Anderson, J., Brune, J., Peng, Z. G., & Vernon, F. L. (2012). A comparison of spectral parameter Kappa from small and moderate earthquakes using Southern California ANZA Seismic Network Data. *Bulletin of the Seismological Society of America, 102*, 284–300.

Ko, Y.-T., Kuo, B.-Y., & Hung, S.-H. (2012). Robust determination of earthquake source parameters and mantle attenuation. *Journal of Geophysical Research, 117*, B04304.

Konno, K., & Ohmachi, T. (1998). Ground-motion characteristics estimated from spectral ratio between horizontal and vertical components of microtremor. *Bulletin of the Seismological Society of America, 88*, 228–241.

Ktenidou, O.-J., Cotton, F., Abrahamson, N. A., & Anderson, J. G. (2014). Taxonomy of κ: A review of definitions and estimation approaches targeted to applications. *Seismological Research Letters, 85*(1), 135–146.

Lawrence, J. F., Cochran, E. S., Chung, A., Kaiser, A., Christensen, C. M., Allen, R., et al. (2014). Rapid earthquake characterization using MEMS Accelerometers and volunteer hosts following the M 7.2 Darfield, New Zealand, earthquake. *Bulletin of the Seismological Society of America, 104*, 184–192.

Liu, Z., Wuenscher, M. E., & Herrmann, R. B. (1994). Attenuation of body waves in the central New Madrid seismic zone. *Bulletin of the Seismological Society of America, 84*(4), 1112–1122.

Loke, M. H., & Dahlin, T. (2002). "A comparison of the Gauss–Newton and quasi-Newton methods in resistivity imaging inversion. *Journal of Applied Geophysics, 49*, 149–162.

Neighbors, C., Liao, E. J., Cochran, E. S., Funning, G. J., Chung, A. I., Lawrence, J. F., et al. (2015). Investigation of the high-frequency Attenuation Parameter, κ (kappa), from aftershocks of the 2010 Mw 8.8 Maule, Chile earthquake. *Geophysical Journal International, 200*(1), 200–215.

Oth, A., Bindi, D., Parolai, S., & Di Giacomo, D. (2010). Earthquake scaling characteristics and the scale (in)dependence of seismic energy-to-moment ratio: Insights from KiK-net data in Japan. *Geophysical Research Letters, 37*(19), L19304.

Oth, A., Bindi, D., Parolai, S., & Di Giacomo, D. (2011). Spectral analysis of K-NET and KiK-net data in Japan, Part II: On attenuation characteristics, source spectra, and site response of borehole and surface stations. *Bulletin of the Seismological Society of America, 101*, 667–687.

Oth, A., & Kaiser, A. E. (2014). Stress release and source scaling of the 2010–2011 Canterbury, New Zealand Earthquake sequence from spectral inversion of ground motion data. *Pure and Applied Geophysics, 171*(10), 2767–2782.

Parolai, S., & Bindi, D. (2004). Influence of soil-layer properties on *k* evaluation. *Bulletin of the Seismological Society of America, 94*, 349–356.

Peterson, T., Gledhill, K., Chadwick, M., Gale, N. H., & Ristau, J. (2011). The New Zealand National Seismograph Network. *Seismological Research Letters, 82*, 9–20.

Purvance, M. D., & Anderson, J. G. (2003). A comprehensive study of the observed spectral decay in strong-motion accelerations recorded in Guerrero, Mexico. *Bulletin of the Seismological Society of America, 93*, 600–611.

Ristau, J. (2013). Update of regional moment tensor analysis for earthquakes in New Zealand and adjacent offshore regions. *Bulletin of the Seismological Society of America, 103*(4), 2520–2533.

Sheen, D.-H., Tuncay, K., Baag, C.-E., & Ortoleva, P. J. (2006). Time domain Gauss–Newton seismic waveform inversion in elastic media. *Geophysical Journal International, 167*(3), 1373–1384.

Sibson, R. H., Ghisetti, F. C., & Ristau, J. (2011). Stress control of an evolving strike-slip fault system during the 2010–2011 Canterbury, New Zealand, earthquake sequence. *Seismological Research Letters, 82*, 824–832.

Taylor, S. R., & Hartse, H. E. (1998). A procedure for estimation of source and propagation amplitude corrections for regional seismic discriminants. *Journal of Geophysical Research, 103*(B2), 2781–2789.

Tsai, C.-C. P., & Chen, K.-C. (2000). A model for the high-cut process of strong-motion accelerations in terms of distance, magnitude, and site condition: An example from the SMART 1 Array, Lotung, Taiwan. *Bulletin of the Seismological Society of America, 200090*, 1535–1542.

Yildirim, B., Cochran, E. S., Chung, A. I., Christensen, C. M., & Lawrence, J. F. (2015). On the reliability of Quake Catcher Network earthquake detections. *Seismological Research Letters, 86*, 856–869.

Zhou, Y., & Kanamori, H. (1987). Regional variation of the short-period (1 to 10 second) source spectrum. *Bulletin of the Seismological Society of America, 77*, 514–529.

(Received February 11, 2016, revised November 10, 2016, accepted November 26, 2016, Published online December 26, 2016)